Placental physiology monitored by hyperpolarized dynamic ^{13}C magnetic resonance

Stefan Markovic[a,1], Anne Fages[a,1], Tangi Roussel[a], Ron Hadas[b], Alexander Brandis[c], Michal Neeman[b,2], and Lucio Frydman[a,2]

[a]Department of Chemical and Biological Physics, Weizmann Institute, 76100 Rehovot, Israel; [b]Department of Biological Regulation, Weizmann Institute, 76100 Rehovot, Israel; and [c]Life Science Core Facilities, Weizmann Institute, 76100 Rehovot, Israel

Edited by David W. Russell, University of Texas Southwestern Medical Center, Dallas, TX, and approved January 22, 2018 (received for review August 27, 2017)

Placental functions, including transport and metabolism, play essential roles in pregnancy. This study assesses such processes in vivo, from a hyperpolarized MRI perspective. Hyperpolarized urea, bicarbonate, and pyruvate were administered to near-term pregnant rats, and all metabolites displayed distinctive behaviors. Little evidence of placental barrier crossing was observed for bicarbonate, at least within the timescales allowed by ^{13}C relaxation. By contrast, urea was observed to cross the placental barrier, with signatures visible from certain fetal organs including the liver. This was further evidenced by the slower decay times observed for urea in placentas vis-à-vis other maternal compartments and validated by mass spectrometric analyses. A clear placental localization, as well as concurrent generation of hyperpolarized lactate, could also be detected for [1-^{13}C]pyruvate. These metabolites also exhibited longer lifetimes in the placentas than in maternal arteries, consistent with a metabolic activity occurring past the trophoblastic interface. When extended to a model involving the administration of a preeclampsia-causing chemical, hyperpolarized MR revealed changes in urea's transport, as well as decreases in placental glycolysis vs. the naïve animals. These distinct behaviors highlight the potential of hyperpolarized MR for the early, minimally invasive detection of aberrant placental metabolism.

pregnancy | placental physiology | hyperpolarized ^{13}C MR | dissolution DNP | preeclamptic models

The placenta is an essential organ that supports the developing embryo by channeling nutrients, respiratory gases, antibodies, and hormones from the maternal to the fetal blood and by clearing fetal waste products back to the maternal circulation (1, 2). Abnormalities in placental function and metabolism are implicated in two thirds of fetal deaths (3). Thus, the early detection of metabolic abnormalities associated with pregnancy complications such as intrauterine growth restriction and preeclampsia (PE) can play a fundamental role in managing predelivery treatments and in taking delivery decisions (4–7). Although ex vivo examination of placentas associated with stillbirths or fetal deaths reveals a great deal about structural and functional abnormalities (8–10), the ability to detect placental dysfunctions noninvasively and in vivo is fundamental for improving the prognosis and treatment of a distressed fetus. Ultrasound examinations are most commonly used in the clinic to detect fetal growth restrictions (11), yet these only detect placental disturbances if the morphological changes associated to the dysfunctions are substantial. Fetal magnetic resonance imaging (MRI) has thus evolved into an established complement to ultrasound, to clarify the nature of fetal abnormalities (12–14). MRI has the potential to identify placental dysfunction by revealing both structural spatial details, as well as dynamic physiological information on flow and metabolism (1, 15). H-based NMR methods have thus been used to shed light on microstructural placental properties (16), to monitor placental/fetal exchanges via water diffusivity experiments (17–19), to probe the oxygenation of the fetoplacental unit by blood oxygen level-dependent methods (20–22), to assess metabolic status via magnetic resonance spectroscopy (16, 23), and to evaluate maternal/fetal blood flows (24–26). Still, given the fact that a fundamental function of placentas is to actively transfer molecules from the maternal to the fetal side in out-of-equilibrium situations, a noninvasive imaging method capable of assessing placental permeability and metabolic activity could give valuable additional insights. Transport-related in vivo assessments are usually achieved by the administration of a tracer; in the case of MRI these could include Gd-containing contrast agents, capable of crossing the maternal–fetal barrier and thereby affect T_1-weighted NMR images. Although placental insufficiencies have been visualized by use of exogenous molecules (27), the use of chelates to visualize metabolites is difficult, and contrast-enhanced clinical MRI studies appear remote due to the potential toxicity of Gd (28). In addition, even in preclinical investigations, different mechanisms will mediate the transport across the placental barrier of endogenous and exogenous molecules, ranging from passive diffusion to active transport trough several cell layers (29). A tool for monitoring transport and metabolic phenomena through the complex maternal/fetal vasculatures meeting in placentas would be most valuable.

This study explores the possibility of monitoring the behavior of different metabolites reaching the placental barrier, via hyperpolarized (HP) ^{13}C MRI and MR spectroscopic imaging (MRSI). Directly monitoring the metabolites in placentas by in

Significance

The placenta mediates the transfer of metabolites and nutrients, and its dysfunction leads to clinical syndromes that jeopardize both the fetus and mother. Current methods for assessing placental transport and metabolism in vivo are limited; the goal of this study is to validate the potential of minimally invasive technologies based on high-sensitivity, hyperpolarized ^{13}C MRI. Distinct placental crossing features were observed when administering different hyperpolarized metabolites to near-term rodents. In particular, [1-^{13}C]pyruvate was observed to clearly localize in the placenta and to efficiently metabolize into lactate in healthy animals. By contrast, though transport appeared normal, a marked decrease in placental metabolism was observed in preeclamptic models. This opens avenues to diagnose placental disorders, which could translate into humans.

Author contributions: S.M., M.N., and L.F. designed research; S.M., A.F., R.H., and A.B. performed research; S.M., A.F., and T.R. contributed new reagents/analytic tools; S.M., A.F., T.R., M.N., and L.F. analyzed data; and L.F. wrote the paper.

The authors declare no conflict of interest.

This article is a PNAS Direct Submission.

[1]S.M. and A.F. contributed equally to this work.

[2]To whom correspondence may be addressed. Email: michal.neeman@weizmann.ac.il or lucio.frydman@weizmann.ac.il.

This article contains supporting information online at www.pnas.org/lookup/suppl/doi:10.1073/pnas.1715175115/-/DCSupplemental.

Published online February 14, 2018.

vivo MR is very challenging, due to the inherently low concentrations of the molecules involved, coupled to the inherent low sensitivity of MR techniques. A recent breakthrough emerged with the introduction of dissolution dynamic nuclear polarization (DNP) (30), a member of a growing family of nuclear hyperpolarization techniques (31, 32) that can increase by up to four orders of magnitude the sensitivity of metabolic magnetic resonance. Dissolution DNP yields, over timescales on the order of the nuclear T_1 (usually a minute or less), dramatic enhancements in the signal-to-noise ratio of ^{13}C-based experiments. During this timescale, metabolites such as urea can be used as agents for monitoring cardiac function (33), blood flow angiography (34, 35), or renal perfusion (36). In addition, a growing field relies on administering HP precursors like [1-^{13}C]pyruvate to monitor metabolism and in particular the rates of glycolytic processes (37–44). Recent work also demonstrated the feasibility of using HP pyruvate to noninvasively examine fetoplacental transport in guinea pigs and chinchillas (45, 46). The present study assesses by HP DNP MR how different metabolites behave in the placentas of naïve and diseased pregnant rats. Distinct behaviors were detected in the ways by which urea and bicarbonate reach the healthy placenta; fetal, placental, and maternal metabolism could also be clearly distinguished with HP [1-^{13}C]pyruvate at late gestational stages. Dynamic ^{13}C MRSI enabled to monitor the spatial localization of these HP metabolites over time, revealing distinct fluxes into the fetoplacental compartments. Furthermore, distinctly different signatures could be detected between healthy placentas and those associated to a preeclamptic rat model.

Methods

Animal Model. All experiments were approved by the Institutional Animal Care and Use Committee of the Weizmann Institute of Science under Protocols 34080217-3 and 36350617-1. Healthy Wistar pregnant rats ($n = 25$) and preeclamptic Wistar rats ($n = 13$) at late pregnancy stages (E17 to E20) were used in this study, with pregnancy timed at E0.5 on the morning following overnight pairing of male/female pairs and after attesting for the mating. A total of $n = 49$ HP ^{13}C MRI/MRSI experiments were recorded on these animals, with the analysis centering mostly on signals from placentas ($n = 58$) and from maternal compartments ($n = 33$). In some cases, the ^{13}C image resolution was increased to enable the analysis of fetal organs (e.g., livers). Rats with PE symptoms were obtained by administration of Nω-Nitro-L-arginine methyl ester hydrochloride (l-NAME) (Sigma–Aldrich) (47, 48). A daily dose of 90–135 mg/kg body weight of l-NAME in PBS was administered either IV or SC from day 14 or 15 of gestation. HP pyruvate and urea injections on these animals ($n = 9$ and $n = 10$, respectively) were started at least 2 d later.

MR Data Acquisition. All experiments were conducted on a 4.7-T Bruker Biospec AV MRI scanner, using a dual-tuned ^{1}H/^{13}C whole-body volume coil (Bruker) in combination with a 20-mm ^{1}H/^{13}C surface coil (Doty Scientific) with active decoupling on the ^{13}C channel. ^{1}H spin-echo (T_2-weighted RARE) and gradient-echo (FLASH) images were recorded before the ^{13}C MR acquisitions for locating the maternal and the fetal organs. Once these maternal compartments—usually kidneys and/or arteries—and units containing the fetuses and the placentas were identified using ^{1}H spin-echo and gradient-echo sequences, HP ^{13}C MRI/MRSI measurements were carried out using one sagittal or two coronal slices (depending on the animal positioning, which was placed sidewise for the former cases and supine for the latter). Hyperpolarization was achieved by microwave irradiation of a glassy sample containing both the radical and the targeted ^{13}C-labeled metabolite, using a 3.35-T Hypersense polarizer (Oxford Instruments). After suitable microwave irradiation the sample was suddenly dissolved, and the resulting HP metabolite was injected into the tail vein of the rodent for subsequent MRSI/MRI acquisitions. These data sets were recorded as a function of time elapsed since injection, using a phase-encoded MRSI sequence based on a centric *k*-sampling scheme preceded by a slice-selective pulse (49), and followed by a free evolution acquisition. Slice thicknesses of 5 or 10 mm containing the relevant maternal and fetoplacental compartments were targeted by these experiments, and 4×4, 5×5, or 6×6 mm^2 in-plane resolution was achieved by sampling 12×12, 10×10, or 8×8 data matrices, respectively. Complete descriptions of the methods involved in the animal handling, metabolites hyperpolarization procedures, MRI experiments, and data processing are given in *SI Appendix*, section 1.

Results

HP ^{13}C-Bicarbonate in Pregnant Rodents. Bicarbonate plays an essential role in pH buffering of tissues, through the CO_2/HCO_3^- equilibrium. To relieve CO_2's acidic by-product effects resulting from fetal respiration, the transport of CO_2 and of bicarbonate across the placenta become important homeostatic factors. Unlike CO_2, which can cross the placental membranes freely, the charged HCO_3^- requires an active carrying performed by a family of anion exchange transporters (50, 51). To investigate this process, 3 mL of 100 mM HP ^{13}C-bicarbonate were injected into the tail vein of pregnant rats ($n = 7$) in E17 to E20 stages. The dynamic ^{13}C images presented in Fig. 1 show prototypical HP ^{13}C-bicarbonate results; additional ^{13}C MRI experiments recorded after the injection of HP ^{13}C-bicarbonate are given in *SI Appendix*, Fig. S2. In general, ^{13}C signals were clearly observed for ∼16 s, with the HP bicarbonate signature being strongest and lasting longest in the maternal arteries. Signals were also observed from placentas, but no responses were detected from fetal organs. Efforts were invested in detecting a potential ^{13}C peak from the CO_2 in the hope of mapping maternal and placental pH in vivo (52, 53), yet no such resonance was visible above the noise despite the presence of carbonic anhydrase in rodents' placentas (54). This was also the case when the sodium salt was replaced by cesium bicarbonate, which being approximately twice as soluble gave substantially stronger HP ^{13}C signals. In all cases, placentas and maternal arteries exhibit intense ^{13}C-bicarbonate signals that undergo a monotonic decay dictated by an average T_1^{eff} of 9.2 ± 1.8 s ($n = 9$) for the maternal kidneys/arteries and of 10.3 ± 1.3 s for the placentas ($n = 10$). Although toxicity due to the

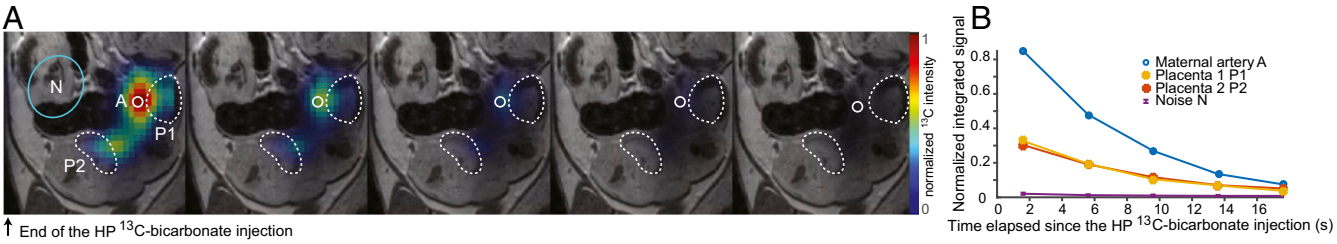

Fig. 1. Representative ^{13}C data obtained following the injection of HP ^{13}C-bicarbonate into a pregnant rat (E19). (*A*) The ^{13}C images (1.5×1.5 mm^2 in-plane resolution, 5 mm slice thickness) recorded after the end of the injection, overlaid on the corresponding middle slice ^{1}H MRI. The white circle shows the maternal artery, and the two dashed curves show materialized placentas from different fetuses. (*B*) The ^{13}C signal intensities integrated over the relevant voxels over the full studied cohort for placentas ($n = 10$) and for maternal (kidney or maternal artery, $n = 9$) compartments. These averaged time courses have signals normalized to the maximum intensity per time curve, and their best fits to a monoexponential function lead to $T_1^{eff} = 10.3 \pm 1.3$ s and 9.2 ± 1.8 s for placental and maternal compartments, respectively.

large amount of cesium injected together with the bicarbonate could have affected these numbers, experiments (n = 3) performed upon ion exchanging the cesium with sodium before the injection to avoid toxicity problems showed similar results. In neither case could transport beyond the placental blood pool—presumably the maternal component of it—be observed.

Urea's Permeability in Pregnant Rodents by HP ^{13}C MRI. Urea crosses the placental layers by passive diffusion as part of the fetal excretory processes (55), making it a good candidate to test HP ^{13}C NMR's usefulness for probing placental permeability. Toward this end, ^{1}H MRI anatomical images were recorded on 10 pregnant rats at late embryonic days (E17 to E20), with suitable fields of view also secured for double-resonance ^{1}H/^{13}C surface coil experiments. Fig. 2*A* shows a representative example of dynamic ^{13}C MRI images collected after the i.v. injection of HP urea through the animal's tail vein. Signals from a maternal kidney and from three distinct placentas are clearly detected, with the ^{13}C-urea signal observable over ca. 45 s. Fig. 2*B* summarizes the dynamic features of these data, as reflected by the ^{13}C signal intensity over time for voxels associated to the maternal kidney and the placentas. In these measurements, maternal kidney exhibits its strongest ^{13}C-urea signal on the first image and then rapidly decays. This behavior was also often observed for other maternal organs, particularly arteries and veins. By contrast the most intense ^{13}C-urea signal within the placentas was usually observed ca. 12 s after the end of the injection, followed by a slower subsequent decay. In general, minor differences in signal intensities also arise between the multiple placentas observed in each HP injection, reflecting the different extent to which these organs were perfused in the experiment and/or captured by the selected slice. Several additional examples of dynamic ^{13}C MRI data collected after the injection of HP ^{13}C-urea are presented in *SI Appendix*, Fig. S2.

To analyze these data, the behaviors seen for the maternal and placental compartments were associated to a simple kinetics given by

$$\frac{d}{dt}U_m = -\frac{U_m}{T_1^{eff}}; \quad \frac{d}{dt}U_p = -\frac{U_p}{T_1^{eff}} + K_{in}\cdot U_m, \qquad [1]$$

where $U_{m,p}$ reflect the signal intensities of urea in the maternal and placental compartments, T_1^{eff} is an effective longitudinal relaxation reflecting the hyperpolarization's decay plus pulse-related magnetization consumption and the vascular washout of the HP metabolite from the compartment of interest, and K_{in} is a kinetic rate reflecting urea's transport from maternal to placental compartments. The solution of this model is presented in *SI Appendix*, section 4, and fits for the time-dependent experiments presented in Fig. 2 and *SI Appendix*, Fig. S3, are given in *SI Appendix*, Fig. S7 and Table S1. Fig. 2*C* summarizes graphically these results, by presenting averages of all of the measurements taken for maternal (n = 12) and placental (n = 10) compartments. The best global fits of these measurements reveal effective decay times T_1^{eff} of 11.3 ± 1.1 s for the maternal and 11.9 ± 0.7 s for the placental compartments. Although these values are slightly shorter than those displayed by ^{13}C-urea in previous in vivo reports (38), the slightly longer lifetimes displayed by placentas probably reflect the faster washout rates occurring in perfused maternal organs such as kidneys and arteries. The experiments also provide best fits for the placental inflow rate: $K_{in} \sim 0.094 \pm 0.014$ s^{-1}.

As complement to these injections on healthy animals, HP urea was injected and monitored on pregnant rats that had been

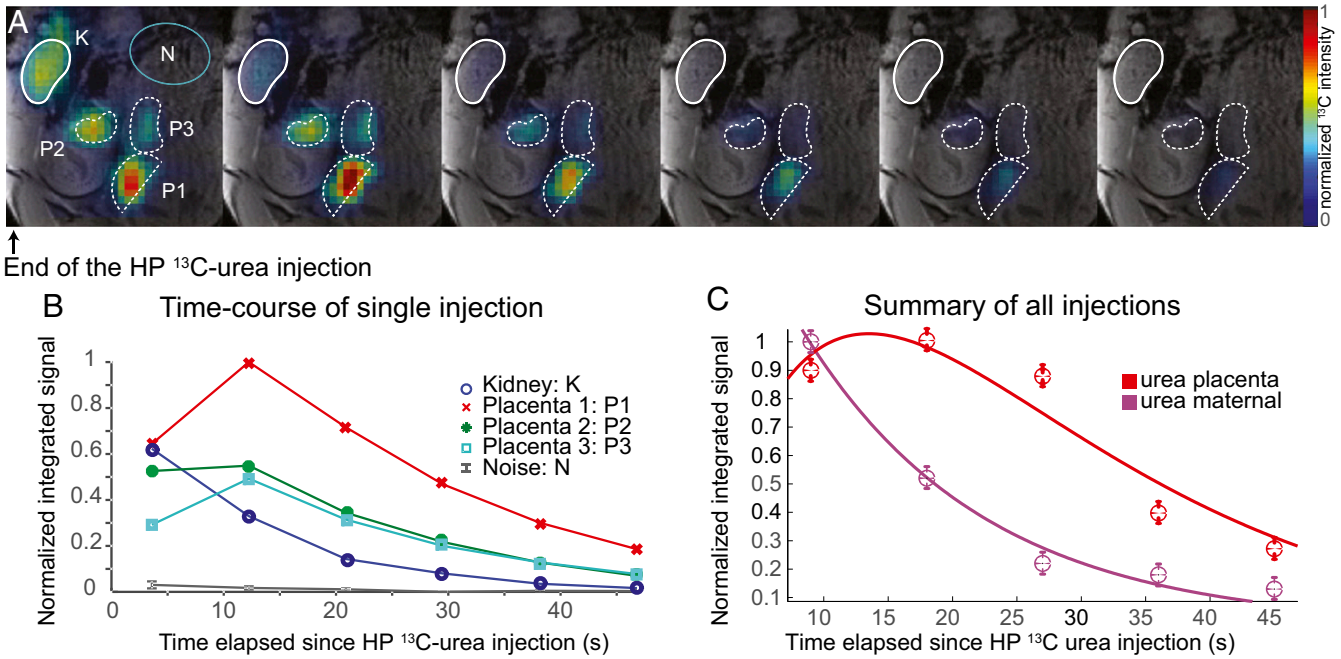

Fig. 2. (*A* and *B*) Representative DNP ^{13}C MRI result observed following the injection of 3 mL of a 115-mM HP ^{13}C-urea solution into a pregnant rat (E19). (*A*) The ^{13}C images (in color) recorded every 7 s on a 5-mm slice with a 1.5 × 1.5 mm^2 in-plane resolution following the injection of a HP sample, overlaid on the corresponding middle slice ^{1}H MRI (gray scale). The rounded white contour (upper left) highlights the maternal kidney, the three lower dashed curves highlight the placentas of different fetuses, and the green oval highlights a region chosen to estimate the ^{13}C NMR noise. (*B*) Quantification of this injection showing the dynamic ^{13}C signal intensities observed for different organs vs. time. All ^{13}C time curves are normalized to the maximum ^{13}C intensity among the different images and were integrated over relevant, indicated voxels. The noise reflects the average ^{13}C signal intensity in the green circle shown on the upper left image. (*C*) Summary of all HP ^{13}C-urea injections observed for placentas (n = 10) and maternal compartments (kidneys and arteries, n = 12) of healthy animals. The points show averaged time course signal normalized to their maximum intensity; the curves show the best fits obtained as described in the text and in *SI Appendix*, section 4, for the placentas and the maternal compartments.

administered l-NAME. The l-NAME–treated animals show symptoms of hypertension, proteinuria, decreased fetal size and litter size, renal damage, intrauterine growth restriction, and TNFα production, which resemble many of the symptoms observed in PE pregnancies (47). These symptoms were recapitulated in the present study, including pups showing truncated limbs as has been reported previously (*SI Appendix*, section 6) (48). Also the anatomic ^{1}H images of pregnant animals subject to l-NAME treatment differed from their naïve counterparts, in that they included placentas exhibiting contrast and anatomical fine structures as seen in healthy animals but also placentas that displayed a darker contrast. These regular and dark-contrast placentas occurred within the same animals, and we attribute the latter's presence to vasculature remodeling effects of the kind that have been previously described on pregnant rabbits subject to l-NAME (56). After giving birth the number of pups observed for these animals was equal to the sum of dark and regular contrast placentas, and they all showed truncated limbs (*SI Appendix*, Fig. S9).

Fig. 3 shows representative ^{13}C MRI results observed upon injecting HP ^{13}C-urea into these PE animals. Repeated experiments (n = 5 animals, n = 16 placentas) revealed an accumulation and eventual decay of the injected metabolite in the placental area but with two distinct kinds of dynamics. For a minority of placentas the buildup/decay processes were as observed for the normal animals, with signals well localized on the organ and lasting on the order of 30–40 s. By contrast a majority of placentas in l-NAME–treated animals showed an intense initial ^{13}C-urea response—approximately twice as strong as for the naïve species—followed by a rapid washout, in a behavior that was reminiscent of the maternal organs. Fig. 3 summarizes some of these features as reflected by selected experiments; a more comprehensive set of results can be found in *SI Appendix*, Fig. S12 and Table S1. Furthermore, inspection of the images revealed for these cases a slight misregistration between the maximum intensity voxel seen in the ^{13}C MRI and the exact placental location in the anatomical ^{1}H data. Overall, this suggests that in the PE model, there is a majority of placentas for which urea arrives but fails to cross the maternal/fetal interface and is thereby rapidly washed away, whereas another subset of placentas exhibits a normal-like urea transport.

In addition to urea signatures from maternal and placental compartments, evidence of ^{13}C-urea in fetal sites was also observed in the healthy animals. *SI Appendix*, Fig. S4, illustrates the presence of urea above the noise level, on positions corresponding to fetal livers. Due to the relative weakness of these ^{13}C signals, the ability of these experiments to quantify urea's in vivo transport into fetuses was limited. To better elucidate this aspect, GC-MS analyses were done on organs and biofluids collected after injection of ^{13}C-urea, on both naïve and l-NAME–treated animals (n = 2 for each). These were killed ca. 1 min after the injection of the labeled urea to mimic the timescales of the DNP MRI experiments; *SI Appendix*, section 2, summarizes the outcome of the isotopic enrichments observed for each kind of animal and for different organs. For normal pregnancies the highest enrichment was observed on the maternal serum with a 1.11 ^{13}C/^{12}C-urea ratio, followed by the maternal kidney (0.62) and the placenta (0.4 ± 0.1). The fetal liver ^{13}C/^{12}C-urea ratio was 0.14 ± 0.03, comparable to the enrichment present in the maternal liver (0.17), whereas the ^{13}C-urea enrichment in the amniotic fluid was 0.09. For l- NAME–treated animals the ^{13}C/^{12}C-urea ratio was 0.2 for maternal kidney, 0.18 ± 0.08 for placentas (n = 5), and 0.07 ± 0.02 for fetal liver (n = 4). These results are consistent with the trends of the in vivo DNP MR experiments because the GC-MS evidences that within the time scale of our experiments, ^{13}C-urea can accumulate in normal placentas and even cross into fetal organs before depolarizing and that a larger scattering and overall lower average of the ^{13}C-urea is found in the placentas and the fetal organs of the PE animals.

The [1-^{13}C]Pyruvate Metabolism in Pregnant Rats. As part of this study we extended investigations that had been previously done with HP pyruvate on pregnant guinea pigs (45), by monitoring the response elicited by HP [1-^{13}C]pyruvate (3 mL, 80 mM) on n = 8 pregnant rats at late gestational days (E17 to E20). Fig. 4 presents a typical ^{13}C MRSI series recorded after the injection of HP pyruvate. The experiment's sensitivity enables one to follow the metabolism of pyruvate to [1-^{13}C]lactate, in both maternal and placental voxels, for over 60 s. In some experiments, [1-^{13}C]alanine could also be detected in the maternal kidney and in the placentas; ^{13}C-bicarbonate could also be observed but without sufficient sensitivity for its localization (*SI Appendix*, Fig. S5). Pyruvate signals (Fig. 4 and *SI Appendix*, Fig. S6) undergo a monotonic decay in the maternal compartments; pyruvate is also readily observable in placentas, where it shows an ∼10-s-long buildup followed by a decay. Pyruvate → lactate production is also sometimes observed in maternal compartments such as kidney; when this is the case, lactate's resonance plateaus ca. 10 s after the HP injection and rapidly decays thereafter. Lactate was much more readily observed in placentas, with a buildup that plateaued ca. 25 s after injection and a decay that is comparable to that in the maternal compartments.

To quantitatively interpret these data, the model in Eq. **1** was expanded to account for the possibility of different pyruvate → lactate metabolic conversion rates in the maternal and placental compartments. This was accounted by the first-order differential equations

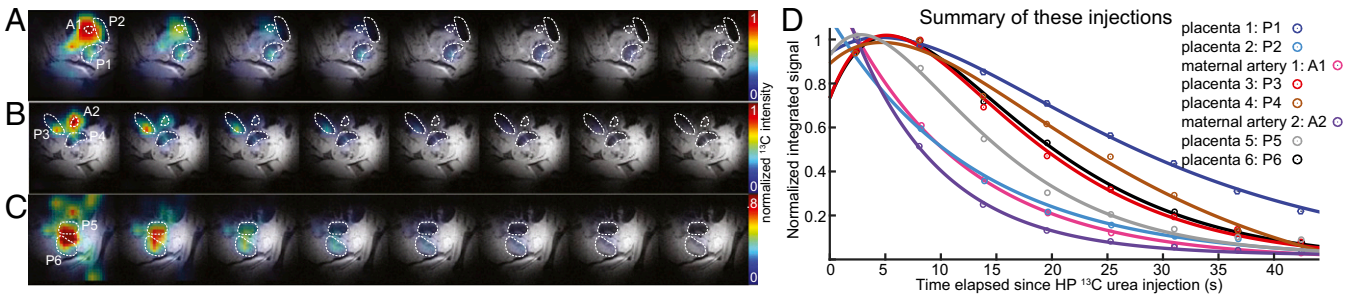

Fig. 3. (*A*–*C*) HP ^{13}C-urea behavior observed for n = 3 pregnant rats treated with l-NAME as described in the text. Highlighted are maternal arteries and a number of placentas showing dissimilar behaviors. (*D*) Time course of the regions indicated in *A*–*C*, normalized to their maximum intensities. Notice the distinctly different behaviors shown by the placentas; that is, in P2 and P5, signals wash away as in the maternal arteries, whereas in P1 and P4 they last for ≥40 s as in the normal cases illustrated in Fig. 2. Unlabeled ^{13}C signals in *C* arise from placentas and other organs, in the periphery of the region detectable with the surface coil used. See *SI Appendix*, section 6, Figs. S11 and S12, and Table S1, for further details of this kinetics.

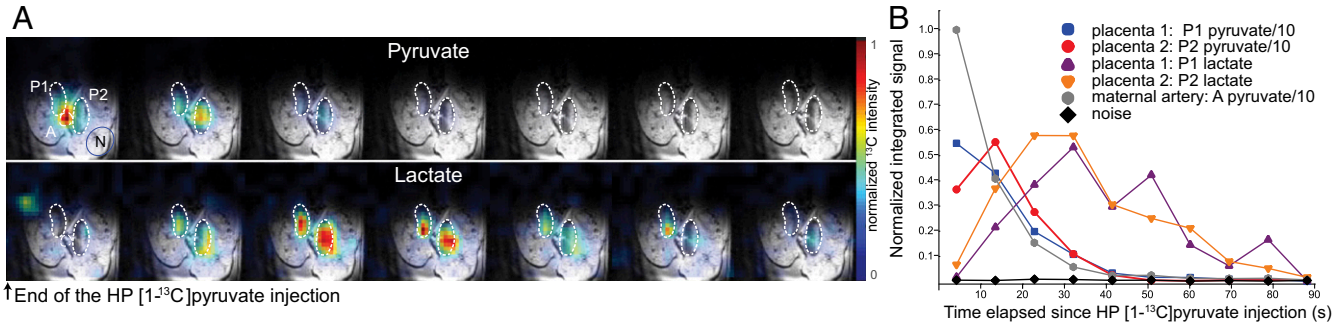

Fig. 4. Representative ^{13}C MRSI data collected every 9 s following the injection of HP [1-^{13}C]pyruvate in a pregnant rat (E20), starting ca. 4 s after completion of the metabolite's injection. (*A*) The ^{13}C MRSI series recorded on a 10-mm-thick slice with a 1.5 × 1.5 mm^2 in-plane resolution, overlaid on the corresponding middle slice ^{1}H NMR image. The upper ^{13}C images arise at the chemical shift of [1-^{13}C]pyruvate and the lower series at the [1-^{13}C]lactate shift. The dashed curves highlight placentas from different fetuses; "A" indicates the strong signal associated to a maternal artery, and "N" indicates a region taken for noise estimation. The top left spot observed in the initial lactate image is centered in one of the maternal kidneys. (*B*) The ^{13}C signal intensities extracted as a function of postinjection time from the voxels highlighted in the ^{13}C images. The lines are meant to help visualizing the changes; signals were normalized as indicated, to fit in a common plot.

$$\frac{d}{dt}P_m = -\frac{P_m}{T_1^p} - K_{metab1}\cdot P_m; \quad \frac{d}{dt}L_m = -\frac{L_m}{T_1^L} + K_{metab1}\cdot P_m$$
$$\frac{d}{dt}P_p = -\frac{P_p}{T_1^p} + K_{in}\cdot P_m - K_{metab}\cdot P_p; \quad \frac{d}{dt}L_p = -\frac{L_p}{T_1^L} + K_{metab}\cdot P_p. \qquad [2]$$

Here $P_{m,p}/L_{m,p}$ reflect the pyruvate/lactate signal intensities emerging from the maternal and placental compartments, respectively; T_1^p/T_1^L are the effective longitudinal decays of pyruvate and lactate that as in previous instances encompass genuine T_1 with pulsing and washout phenomena; K_{in} is a rate reflecting pyruvate's transport into the placenta; and K_{metab1}/K_{metab} are the kinetics governing the Pyruvate → Lactate conversion in maternal/placental compartments respectively, rates which in principle we allowed to differ. Solutions for the time-dependent intensities $\{P_m, P_p, L_m, L_p\}$ predicted by these equations are given in *SI Appendix*, section 5, which also illustrates in *SI Appendix*, Fig. S8 and Table S2, the best fits that these solutions gave for data arising from numerous measurements in independent maternal and fetal compartments, respectively. Fig. 5 summarizes these results, by presenting the animal-averaged kinetics of the [1-^{13}C]pyruvate and [1-^{13}C]lactate signals arising from placental and maternal compartments. These time traces indicate that ca. 25% of the maximum maternal pyruvate translocates into the placenta at a rate $K_{in} = 0.21 \pm 0.03$ s^{-1} and that the resulting pyruvate is metabolized into lactate at a rate $K_{metab} = 0.085 \pm 0.008$ s^{-1}. This is slightly slower that the 0.14 s^{-1} rate found for maternal compartments, even if the uncertainty in the latter was difficult to assess. All data could be satisfactorily fitted using $T_1^p \sim 28 \pm 3$ s and $T_1^L \sim 20.5 \pm 2$ s; these are slightly shorter T_1 times than literature values cited in vivo for pyruvate and lactate (57), probably reflecting the effects of pulsing and outflow in these systems. When considering the various variables that could affect the experiment also here, as with the urea, there is a remarkable consistency in the absolute pyruvate signal intensity associated to the fits.

HP [1-^{13}C]pyruvate was also monitored on pregnant rats that had been subject to the l-NAME treatment. By contrast to the urea case, these injections showed similar placental pyruvate intensities and time courses as observed in healthy animals. However, although the bolus of HP pyruvate appeared to reach the PE placentas in normal times and amounts, the levels of HP ^{13}C-lactate observed in these placentas turned out notably lower. In fact, dynamic analyses using time traces of the kind shown in Fig. 5 were only possible in a single case; in all other instances the HP lactate sensitivity was insufficient to discern the intensities of multiple data points. This successful dataset showed lactate peaking ca. 20–25 s after the hyperpolarized injection (Fig. 6 *A* and *B*), a timescale that coincides with the one seen in healthy animals. Fitting these data revealed K_{in}, K_{metab}, and *Pyr* parameters on the lower-end range of what had been observed for healthy animals (*SI Appendix*, Table S2). Although similar kinetic analyses were not possible on the remaining datasets, sensitivity could be sufficiently enhanced by averaging together all of the postinjection images observed for the lactate resonance. This allowed us to determine the overall ^{13}C-lactate and ^{13}C-pyruvate intensities; *SI Appendix*, Fig. S13, shows these averaged images for $n = 8$ l-NAME–treated animals. This in turn allowed us to calculate the lactate/total carbon ratio for the different PE placentas and compare these signal intensity ratios with values derived from the data collected on healthy controls. The HP data revealed a significant difference in the glycolytic rates of the l-NAME–treated animals, with total_lactate/total_Carbon ratios shifting from 0.18 ± 0.03 for healthy placentas to 0.050 ± 0.033 in PE ones (Fig. 6*C*). This is a significant drop, which might in principle be associated with changes in placental perfusion associated to the administration of l-NAME, a chemical known to inhibit NO production. Upon comparing the total amount of hyperpolarized ^{13}C signals emanating from

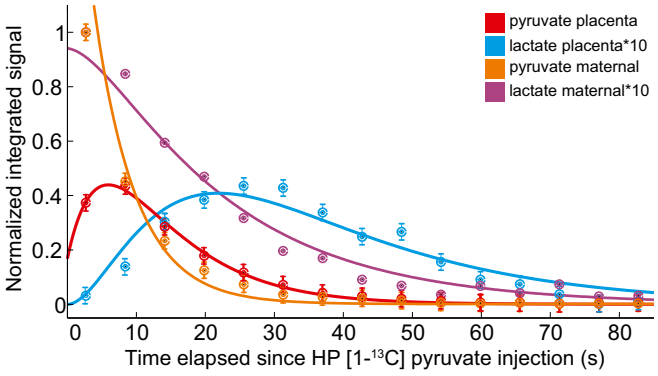

Fig. 5. Average ^{13}C signal intensities observed in $n = 5$ dissolution DNP MRSI experiments showing the progression and best fit of the pyruvate and lactate intensities in the maternal and placental compartments of naïve rats. Spectral intensities have been multiplied by the factors indicated in *Inset* to fit a common scale. See text and *SI Appendix*, section 5, for further details.

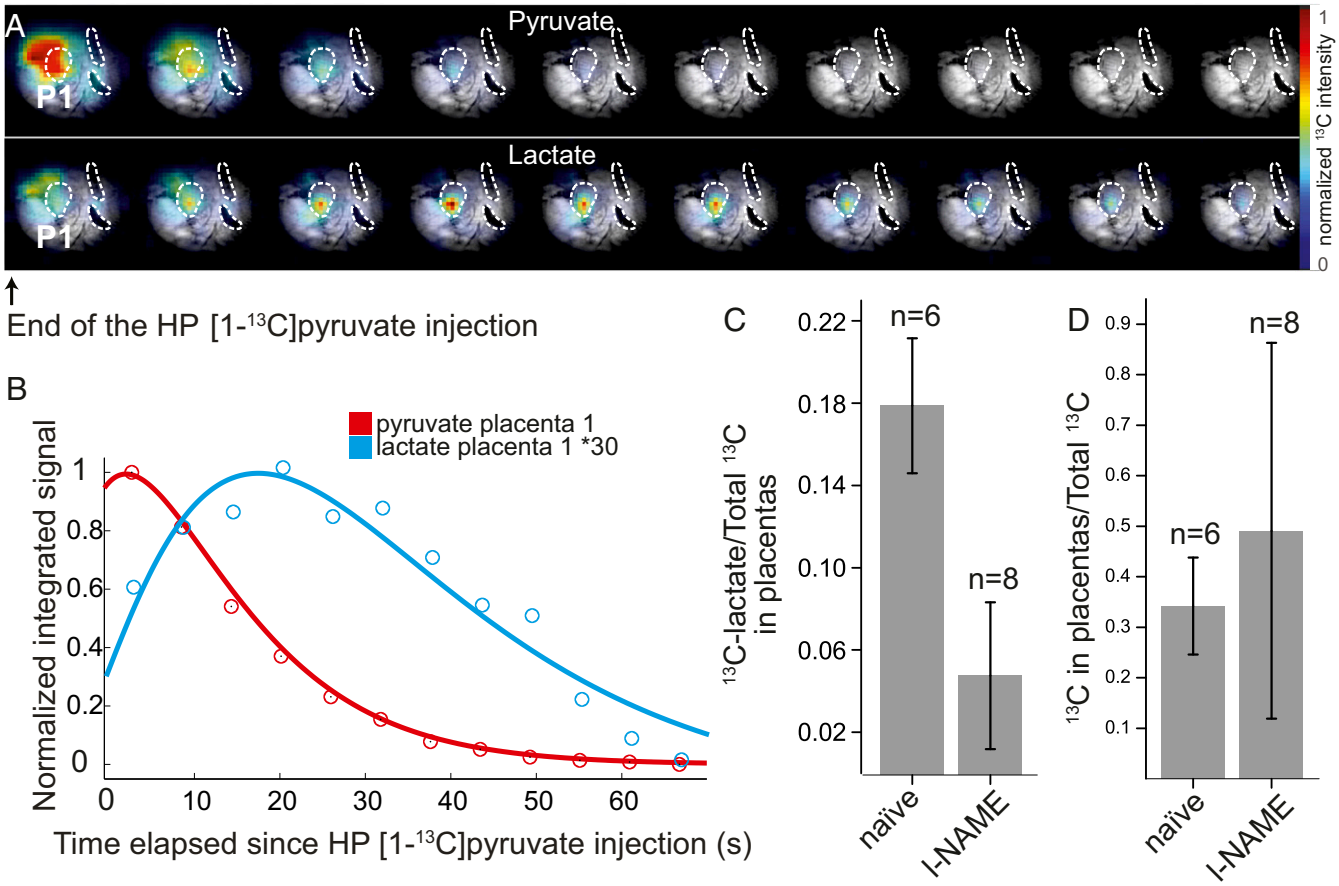

Fig. 6. HP ^{13}C MRSI data collected on l-NAME–treated pregnant rats. (*A*) Pyruvate and lactate images collected 5 s apart following the injection of HP [1-^{13}C]pyruvate in a pregnant rat (E18), starting ca. 4 s after completion of the metabolite's injection. The ^{13}C MRSI sets were recorded on a 10-mm-thick slice with a 1.5 × 1.5 mm^2 in-plane resolution and are shown overlaid on the corresponding anatomical ^{1}H MRI slice (obtained from the surface coil). The three dashed curves highlight placentas from different fetuses; P1, the placenta that exhibits the highest ^{13}C signal intensity, was used for the analysis shown in *B*. (*B*) The ^{13}C signal intensities extracted as a function of postinjection time from the voxel highlighted in the ^{13}C images. The lines are best fits determined as described in the text and summarized in *SI Appendix*, Table S2. (*C*) Summary of the signal intensity ratios between the [1-^{13}C]lactate and the total ^{13}C signals integrated from placentas for naïve and l-NAME–treated rats, with $n = 6$ (naïve) and $n = 8$ (l-NAME) separate injections. (*D*) Idem as in *C* but upon comparing the ratios between total hyperpolarized ^{13}C signals arising from within and from (within + without) placentas, in the same animal cohort.

within and from outside the placentas in animals that were subject to this chemical from animals that were not, no significant restrictions on flow through the placentas could be noticed (Fig. 6*D*).

Discussion

Placental functions, including passive and active transports and a semiautonomous metabolism, play essential roles throughout a pregnancy. Placentas mediate the exchanges of maternal blood nutrients and of gases and the clearing of fetal waste, and are involved in metabolic homeostasis. Throughout a pregnancy, the increasing needs of the fetus are satisfied by changes in placental vasculature; this maturation involves both blood vessel growth due to angiogenesis and relaxation of the vessels due to loss of vascular smooth muscle cells (58). Placental maturation is paralleled by an increase in surface area, which is in turn associated with the development of a more complex villiar structure. Lying at the center of these structures and dynamics are the giant trophoblast cells, which mediate the exchanges of nutrients and waste between the fetal capillaries and the maternal blood pools.

The purpose of this work was to assess in vivo aspects of how metabolites behave throughout these various placental layers, as viewed through the administration of HP ^{13}C-urea, ^{13}C-bicarbonate, and [1-^{13}C]pyruvate. These experiments were performed at late embryonic stages (E17–E20, just short of delivery), to benefit from the easier imaging and kinetic measurement conditions posed by larger fetuses and more mature placentas. Working at these late gestation days, all three of the examined metabolites displayed distinctive behaviors. Within the timescales allowed by the loss of hyperpolarization, urea was observed to reach the placenta and even cross its barrier, with signatures visible from certain fetal organs like liver. This suggests an active transport aiding the free diffusion and a full crossing through the placental trophoblasts. The slightly slower decay times observed for HP urea in placentas vis-à-vis maternal counterparts such as kidneys could reflect the fact that the former signals originate both from the highly perfused maternal blood pools of the placentas and from fetal capillaries present in the placental labyrinths (9). This dynamics appeared affected in the l-NAME–treated animals, for which some placentas evidenced a fast washout of the HP urea, hinting at a precluded crossing from the maternal to the fetal side. The invasive but more sensitive mass spectrometric analyses that were performed to quantify ^{13}C/^{12}C-urea ratios in various harvested organs (*SI Appendix*, section 2) provided independent validation for the estimations afforded by the in vivo MR measurements. Notice that these placental barrier-crossing measurements are opposite to those which would naturally occur because urea is a waste product normally traversing the placental barrier

from the fetal to the maternal side. Still, being a neutral, small molecule, this crossing would be driven by concentration gradients through the cell layers making up the placental barrier. For instance, aquaporins, water channels that increase permeability of lipid membranes in response to osmotic or hydrostatic gradients and which are present in the placental trophoblasts, are also permeable to urea (59–61). The maternal → placental → fetal urea translocation observed by HP MRI is therefore likely to give insight into the in vivo rates of opposite barrier crossings as well.

By contrast to urea's behavior, little or no evidence of placental barrier crossing during the timescale of the experiments was observed for bicarbonate. This could reflect to some extent the limitations imposed by bicarbonate's faster depolarization (53); yet even within these boundaries, differences arose between the transport exhibit by this anion and that exhibited by urea. In fact, the nearly identical decay rates evidenced by maternal and placental compartments suggest that within the timescales afforded by hyperpolarization, bicarbonate remains mostly in the maternal blood pool. Furthermore, although HP ^{13}C-bicarbonate could provide insight about in vivo pH, we failed to detect the HP $^{13}CO_2$ peak needed to perform such measurements. Adding to this weakness was our inability to find a suitable mass spectrometry protocol for accurately quantifying the presence of labeled bicarbonate in harvested organs, owing to this molecule's volatility.

However, a third, distinct behavior was evidenced by [1-^{13}C]pyruvate. In this case a clear localization in the placentas could be detected—much clearer than in most of the maternal organs and to some extent clearer than that reported by previous DNP MRSI experiments on guinea pigs (45). Aiding these observation is the approximately threefold faster intravasation rate K_{in} that HP pyruvate shows over urea, reflecting in all likelihood the action of GLUT transporters that assist the former but not the latter. Evident as well was the generation of lactate from the HP pyruvate within the placenta, a pool that, judging by its considerable lifetime, is protected from the washout effects that one could expect from the rapid maternal or even fetal perfusion occurring within the organ. Indeed, within the assessed timescales, products that are in fast exchange with the small but rapidly perfused fetal blood pool would wash out of the placenta and reveal themselves into fetal organs. Because little evidence for either [1-^{13}C]pyruvate or [1-^{13}C]lactate appears in fetal organs, it seems that the active generation of lactate observed in placentas is a product of metabolic activity within the trophoblastic cells themselves. The average rate K_{metab} observed for the pyruvate → lactate conversion process in healthy placentas was ~0.08 s^{-1}, similar to that reported for active muscles or tumors (49, 62, 63). Notably, this conversion process was found to be highly sensitive to l-NAME–derived placental dysfunctions, boding well for the potential of this technique in the characterization of placental metabolism and for the diagnosis of PE-like diseases based on hyperpolarized MR. Although the exact nature of these observed metabolic changes remain to be discerned, measurements associated to the distribution of the hyperpolarized ^{13}C labels suggest that this discerning contrast is not related to changes in placental perfusion of the injected pyruvate.

Conclusions

Noninvasive identification and characterization of placental function is a main challenge in obstetrics. In this preclinical study, the administration of ^{13}C-labeled metabolites and their monitoring by HP MRI and MRSI provided distinct insights into placental physiology for the various species. The rich perfusion and considerable permeability characteristic of placentas surely contributed to the rapid localization of the hyperpolarized compounds in these units; these high-vascularity and high-perfusion features are preserved in human placentas, which like their rodent counterparts share a hemochoriality that puts maternal blood in direct contact with the outer fetal membrane. This bodes well for extending this kind of minimally invasive assessments into the clinic. Also promising was the clear discrimination that HP precursors could make between normal and abnormal placentas because the PE models revealed differences both in the urea uptake and in the conversion of [1-^{13}C]pyruvate into lactate. On the other hand, other valuable goals, like the mapping of metabolism for different fetal organs and the determination of in vivo placental pH, could not be achieved. Ongoing efforts also include a more detailed characterization on the origins of the metabolic changes observed in a PE model, including more complex experiments that combine HP, diffusivity and contrast perfusion MR measurements. Studies have also begun to investigate other pregnancy-related dysfunction models in rodents (48, 64, 65) and tests in human placenta explants of normal and high-risk pregnancies.

ACKNOWLEDGMENTS. We are grateful to Dr. Veronica Frydman for the preparation of the ^{13}C-labeled cesium bicarbonate, to Dr. Greg Olsen and Koby Zibzener for assistance with the hyperpolarizer, and to Dr. Nava Nevo and Marina Lysenko (Weizmann Institute) for their help in preparing and handling the animals. We also thank Prof. Joel Garbow (Washington University) for valuable discussions. A.F. acknowledges the French Ministry of Foreign Affairs for an International Volunteers Program postdoctoral fellowship. This research was supported by Minerva Project 712277, NIH Grant R01HD086323, the Kimmel Institute for Magnetic Resonance (Weizmann Institute), and the generosity of the Perlman Family Foundation.

1. Benirschke K, Burton GJ, Baergen RN (2012) *Pathology of the Human Placenta* (Springer, New York).
2. Kay H, Nelson M, Wamg Y (2011) *The Placenta: From Development to Disease* (John Wiley and Sons, Hoboken, NJ).
3. Korteweg FJ, et al. (2009) Diverse placental pathologies as the main causes of fetal death. *Obstet Gynecol* 114:809–817.
4. Chaiworapongsa T, Chaemsaithong P, Yeo L, Romero R (2014) Pre-eclampsia part 1: Current understanding of its pathophysiology. *Nat Rev Nephrol* 10:466–480.
5. Kingdom JCP, Kaufmann P (1997) Oxygen and placental villous development: Origins of fetal hypoxia. *Placenta* 18:613–621, discussion 623–626.
6. Mayhew TM, Manwani R, Ohadike C, Wijesekara J, Baker PN (2007) The placenta in pre-eclampsia and intrauterine growth restriction: Studies on exchange surface areas, diffusion distances and villous membrane diffusive conductances. *Placenta* 28: 233–238.
7. Zhang S, et al. (2015) Placental adaptations in growth restriction. *Nutrients* 7:360–389.
8. Chen CP, Bajoria R, Aplin JD (2002) Decreased vascularization and cell proliferation in placentas of intrauterine growth-restricted fetuses with abnormal umbilical artery flow velocity waveforms. *Am J Obstet Gynecol* 187:764–769.
9. Macara L, et al. (1996) Structural analysis of placental terminal villi from growth-restricted pregnancies with abnormal umbilical artery Doppler waveforms. *Placenta* 17:37–48.
10. Rayburn W, Sander C, Barr M, Jr, Rygiel R (1985) The stillborn fetus: Placental histologic examination in determining a cause. *Obstet Gynecol* 65:637–641.
11. Abramowicz JS, Sheiner E (2008) Ultrasound of the placenta: A systematic approach. Part I: Imaging. *Placenta* 29:225–240.
12. Blaicher W, et al. (2006) Magnetic resonance imaging of the normal placenta. *Eur J Radiol* 57:256–260.
13. Levine D, Barnes PD, Edelman RR (1999) Obstetric MR imaging. *Radiology* 211: 609–617.
14. Levine D, Barnes PD, Madsen JR, Li W, Edelman RR (1997) Fetal central nervous system anomalies: MR imaging augments sonographic diagnosis. *Radiology* 204:635–642.
15. Avni R, Neeman M, Garbow JR (2015) Functional MRI of the placenta–From rodents to humans. *Placenta* 36:615–622.
16. Denison FC, et al. (2012) Novel use of proton magnetic resonance spectroscopy (1HMRS) to non-invasively assess placental metabolism. *PLoS One* 7:e42926.
17. Moore RJ, et al. (2000) In vivo intravoxel incoherent motion measurements in the human placenta using echo-planar imaging at 0.5 T. *Magn Reson Med* 43: 295–302.
18. Morita S, et al. (2009) Feasibility of diffusion-weighted MRI for defining placental invasion. *J Magn Reson Imaging* 30:666–671.
19. Solomon E, et al. (2014) Major mouse placental compartments revealed by diffusion-weighted MRI, contrast-enhanced MRI, and fluorescence imaging. *Proc Natl Acad Sci USA* 111:10353–10358.
20. Aimot-Macron S, et al. (2013) In vivo MRI assessment of placental and foetal oxygenation changes in a rat model of growth restriction using blood oxygen level-dependent (BOLD) magnetic resonance imaging. *Eur Radiol* 23:1335–1342.

21. Avni R, et al. (2016) MR imaging-derived oxygen-hemoglobin dissociation curves and fetal-placental oxygen-hemoglobin affinities. *Radiology* 280:68–77.
22. Chalouhi GE, et al. (2013) Fetoplacental oxygenation in an intrauterine growth restriction rat model by using blood oxygen level-dependent MR imaging at 4.7 T. *Radiology* 269:122–129.
23. Sohlberg S, et al. (2014) In vivo ^{31}P-MR spectroscopy in normal pregnancy, early and late preeclampsia: A study of placental metabolism. *Placenta* 35:318–323.
24. Francis ST, et al. (1998) Non-invasive mapping of placental perfusion. *Lancet* 351: 1397–1399.
25. Gowland PA, et al. (1998) In vivo perfusion measurements in the human placenta using echo planar imaging at 0.5 T. *Magn Reson Med* 40:467–473.
26. Remus CC, et al. (2013) Application of the steepest slope model reveals different perfusion territories within the mouse placenta. *Placenta* 34:899–906.
27. Taillieu F, et al. (2006) Placental perfusion and permeability: Simultaneous assessment with dual-echo contrast-enhanced MR imaging in mice. *Radiology* 241:737–745.
28. Ramalho J, et al. (2016) Gadolinium-based contrast agent accumulation and toxicity: An update. *AJNR Am J Neuroradiol* 37:1192–1198.
29. Sibley CP, et al. (1998) Mechanisms of maternofetal exchange across the human placenta. *Biochem Soc Trans* 26:86–91.
30. Golman K, in 't Zandt R, Thaning M (2006) Real-time metabolic imaging. *Proc Natl Acad Sci USA* 103:11270–11275.
31. Ardenkjaer-Larsen J-H, et al. (2015) Facing and overcoming sensitivity challenges in biomolecular NMR spectroscopy. *Angew Chem Int Ed Engl* 54:9162–9185.
32. Budker D, Kimball DFJ (2013) *Optical Magnetometry* (Cambridge Univ Press, Cambridge, UK).
33. Lau AZ, Miller JJ, Robson MD, Tyler DJ (2016) Cardiac perfusion imaging using hyperpolarized (13)C urea using flow sensitizing gradients. *Magn Reson Med* 75: 1474–1483.
34. Reed GD, et al. (2014) High resolution (^{13})C MRI with hyperpolarized urea: In vivo T(2) mapping and (15)N labeling effects. *IEEE Trans Med Imaging* 33:362–371.
35. von Morze C, et al. (2011) Imaging of blood flow using hyperpolarized [(13)C]urea in preclinical cancer models. *J Magn Reson Imaging* 33:692–697.
36. von Morze C, Bok RA, Sands JM, Kurhanewicz J, Vigneron DB (2012) Monitoring urea transport in rat kidney in vivo using hyperpolarized ^{13}C magnetic resonance imaging. *Am J Physiol Renal Physiol* 302:F1658–F1662.
37. Brindle KM (2015) Imaging metabolism with hyperpolarized (13)C-labeled cell substrates. *J Am Chem Soc* 137:6418–6427.
38. Golman K, Ardenkjaer-Larsen JH, Petersson JS, Mansson S, Leunbach I (2003) Molecular imaging with endogenous substances. *Proc Natl Acad Sci USA* 100:10435–10439.
39. Golman K, Zandt RI, Lerche M, Pehrson R, Ardenkjaer-Larsen JH (2006) Metabolic imaging by hyperpolarized ^{13}C magnetic resonance imaging for in vivo tumor diagnosis. *Cancer Res* 66:10855–10860.
40. Harris T, Degani H, Frydman L (2013) Hyperpolarized ^{13}C NMR studies of glucose metabolism in living breast cancer cell cultures. *NMR Biomed* 26:1831–1843.
41. Kurhanewicz J, et al. (2011) Analysis of cancer metabolism by imaging hyperpolarized nuclei: Prospects for translation to clinical research. *Neoplasia* 13:81–97.
42. Nonaka H, et al. (2013) A platform for designing hyperpolarized magnetic resonance chemical probes. *Nat Commun* 4:2411.
43. Rodrigues TB, et al. (2014) Magnetic resonance imaging of tumor glycolysis using hyperpolarized 13C-labeled glucose. *Nat Med* 20:93–97.
44. Schroeder MA, Clarke K, Neubauer S, Tyler DJ (2011) Hyperpolarized magnetic resonance: A novel technique for the in vivo assessment of cardiovascular disease. *Circulation* 124:1580–1594.
45. Friesen-Waldner LJ, et al. (2016) Hyperpolarized [1-(13) C]pyruvate MRI for non-invasive examination of placental metabolism and nutrient transport: A feasibility study in pregnant Guinea pigs. *J Magn Reson Imaging* 43:750–755.
46. Mikkelsen E, et al. (2017) The chinchilla as a novel animal model of pregnancy. *R Soc Open Sci* 4:161098.
47. Souza CO, et al. (2012) Hepatoprotective and anti-inflammatory effects of silibinin on experimental preeclampsia induced by L-NAME in rats. *Life Sci* 91:159–165.
48. Fantel AG, Person RE (2002) Involvement of mitochondria and other free radical sources in normal and abnormal fetal development. *Ann N Y Acad Sci* 959:424–433.
49. Leftin A, Roussel T, Frydman L (2014) Hyperpolarized functional magnetic resonance of murine skeletal muscle enabled by multiple tracer-paradigm synchronizations. *PLoS One* 9:e96399.
50. Bonar PT, Casey JR (2008) Plasma membrane Cl^-/HCO_3^- exchangers: Structure, mechanism and physiology. *Channels (Austin)* 2:337–345.
51. Grassl SM (1989) C1/HCO3 exchange in human placental brush border membrane vesicles. *J Biol Chem* 264:11103–11106.
52. Gallagher FA, Kettunen MI, Brindle KM (2011) Imaging pH with hyperpolarized 13C. *NMR Biomed* 24:1006–1015.
53. Gallagher FA, et al. (2008) Magnetic resonance imaging of pH in vivo using hyperpolarized 13C-labelled bicarbonate. *Nature* 453:940–943.
54. Lutwak-Mann C (1955) Carbonic anhydrase in the female reproductive tract; occurrence, distribution and hormonal dependence. *J Endocrinol* 13:26–38.
55. Sands JM (2003) Molecular mechanisms of urea transport. *J Membr Biol* 191:149–163.
56. Lecarpentier E, et al. (2012) Quantification of utero-placental vascularization in a rabbit model of IUGR with three-dimensional power Doppler angiography. *Placenta* 33:769–775.
57. Zierhut ML, et al. (2010) Kinetic modeling of hyperpolarized 13C1-pyruvate metabolism in normal rats and TRAMP mice. *J Magn Reson* 202:85–92.
58. Cross JC, et al. (2002) Trophoblast functions, angiogenesis and remodeling of the maternal vasculature in the placenta. *Mol Cell Endocrinol* 187:207–212.
59. Damiano A, Zotta E, Goldstein J, Reisin I, Ibarra C (2001) Water channel proteins AQP3 and AQP9 are present in syncytiotrophoblast of human term placenta. *Placenta* 22:776–781.
60. Liu H, Zheng Z, Wintour EM (2008) Aquaporins and fetal fluid balance. *Placenta* 29: 840–847.
61. Sha XY, Xiong ZF, Liu HS, Di XD, Ma TH (2011) Maternal-fetal fluid balance and aquaporins: From molecule to physiology. *Acta Pharmacol Sin* 32:716–720.
62. Leftin A, Degani H, Frydman L (2013) In vivo magnetic resonance of hyperpolarized [(13)C1]pyruvate: Metabolic dynamics in stimulated muscle. *Am J Physiol Endocrinol Metab* 305:E1165–E1171.
63. Swisher CL, et al. (2014) Quantitative measurement of cancer metabolism using stimulated echo hyperpolarized carbon-13 MRS. *Magn Reson Med* 71:1–11.
64. Mayhew TM, Charnock-Jones DS, Kaufmann P (2004) Aspects of human fetoplacental vasculogenesis and angiogenesis. III. Changes in complicated pregnancies. *Placenta* 25:127–139.
65. Omo-Aghoja L (2014) Maternal and fetal acid-base chemistry: A major determinant of perinatal outcome. *Ann Med Health Sci Res* 4:8–17.